LETTERS

Understanding individual human mobility patterns

Marta C. González[1], César A. Hidalgo[1,2] & Albert-László Barabási[1,2,3]

Despite their importance for urban planning[1], traffic forecasting[2] and the spread of biological[3–5] and mobile viruses[6], our understanding of the basic laws governing human motion remains limited owing to the lack of tools to monitor the time-resolved location of individuals. Here we study the trajectory of 100,000 anonymized mobile phone users whose position is tracked for a six-month period. We find that, in contrast with the random trajectories predicted by the prevailing Lévy flight and random walk models[7], human trajectories show a high degree of temporal and spatial regularity, each individual being characterized by a time-independent characteristic travel distance and a significant probability to return to a few highly frequented locations. After correcting for differences in travel distances and the inherent anisotropy of each trajectory, the individual travel patterns collapse into a single spatial probability distribution, indicating that, despite the diversity of their travel history, humans follow simple reproducible patterns. This inherent similarity in travel patterns could impact all phenomena driven by human mobility, from epidemic prevention to emergency response, urban planning and agent-based modelling.

Given the many unknown factors that influence a population's mobility patterns, ranging from means of transportation to job- and family-imposed restrictions and priorities, human trajectories are often approximated with various random walk or diffusion models[7,8]. Indeed, early measurements on albatrosses[9], followed by more recent data on monkeys and marine predators[10,11], suggested that animal trajectory is approximated by a Lévy flight[12,13]—a random walk for which step size Δr follows a power-law distribution $P(\Delta r) \sim \Delta r^{-(1+\beta)}$, where the displacement exponent $\beta < 2$. Although the Lévy statistics for some animals require further study[14], this finding has been generalized to humans[7], documenting that the distribution of distances between consecutive sightings of nearly half-a-million bank notes is fat-tailed. Given that money is carried by individuals, bank note dispersal is a proxy for human movement, suggesting that human trajectories are best modelled as a continuous-time random walk with fat-tailed displacements and waiting-time distributions[7]. A particle following a Lévy flight has a significant probability to travel very long distances in a single step[12,13], which seems to be consistent with human travel patterns: most of the time we travel only over short distances, between home and work, whereas occasionally we take longer trips.

Each consecutive sighting of a bank note reflects the composite motion of two or more individuals who owned the bill between two reported sightings. Thus, it is not clear whether the observed distribution reflects the motion of individual users or some previously unknown convolution between population-based heterogeneities and individual human trajectories. Contrary to bank notes, mobile phones are carried by the same individual during his/her daily routine, offering the best proxy to capture individual human trajectories[15–19].

We used two data sets to explore the mobility pattern of individuals. The first (D_1) consisted of the mobility patterns recorded over a six-month period for 100,000 individuals selected randomly from a sample of more than 6 million anonymized mobile phone users. Each time a user initiated or received a call or a text message, the location of the tower routeing the communication was recorded, allowing us to reconstruct the user's time-resolved trajectory (Fig. 1a, b). The time between consecutive calls followed a 'bursty' pattern[20] (see Supplementary Fig. 1), indicating that although most consecutive calls are placed soon after a previous call, occasionally there are long periods without any call activity. To make sure that the obtained results were not affected by the irregular call pattern, we also studied a data set (D_2) that captured the location of 206 mobile phone users, recorded every two hours for an entire week. In both data sets, the spatial resolution was determined by the local density of the more than 10^4 mobile towers, registering movement only when the user moved between areas serviced by different towers. The average service area of each tower was approximately 3 km^2, and over 30% of the towers covered an area of 1 km^2 or less.

To explore the statistical properties of the population's mobility patterns, we measured the distance between user's positions at consecutive calls, capturing 16,264,308 displacements for the D_1 and 10,407 displacements for the D_2 data set. We found that the distribution of displacements over all users is well approximated by a truncated power-law:

$$P(\Delta r) = (\Delta r + \Delta r_0)^{-\beta} \exp(-\Delta r/\kappa) \quad (1)$$

with exponent $\beta = 1.75 \pm 0.15$ (mean $\pm$ standard deviation), $\Delta r_0 = 1.5$ km and cutoff values $\kappa|_{D_1} = 400$ km and $\kappa|_{D_2} = 80$ km (Fig. 1c, see the Supplementary Information for statistical validation). Note that the observed scaling exponent is not far from $\beta = 1.59$ observed in ref. 7 for bank note dispersal, suggesting that the two distributions may capture the same fundamental mechanism driving human mobility patterns.

Equation (1) suggests that human motion follows a truncated Lévy flight[7]. However, the observed shape of $P(\Delta r)$ could be explained by three distinct hypotheses: first, each individual follows a Lévy trajectory with jump size distribution given by equation (1) (hypothesis A); second, the observed distribution captures a population-based heterogeneity, corresponding to the inherent differences between individuals (hypothesis B); and third, a population-based heterogeneity coexists with individual Lévy trajectories (hypothesis C); hence, equation (1) represents a convolution of hypotheses A and B.

To distinguish between hypotheses A, B and C, we calculated the radius of gyration for each user (see Supplementary Information), interpreted as the characteristic distance travelled by user a when observed up to time t (Fig. 1b). Next, we determined the radius of gyration distribution $P(r_g)$ by calculating r_g for all users in samples D_1 and D_2, finding that they also can be approximated with a truncated power-law:

$$P(r_g) = \left(r_g + r_g^0\right)^{-\beta_r} \exp(-r_g/\kappa) \quad (2)$$

[1]Center for Complex Network Research and Department of Physics, Biology and Computer Science, Northeastern University, Boston, Massachusetts 02115, USA. [2]Center for Complex Network Research and Department of Physics and Computer Science, University of Notre Dame, Notre Dame, Indiana 46556, USA. [3]Center for Cancer Systems Biology, Dana Farber Cancer Institute, Boston, Massachusetts 02115, USA.

©2008 Nature Publishing Group

with $r_g^0 = 5.8$ km, $\beta_r = 1.65 \pm 0.15$ and $\kappa = 350$ km (Fig. 1d, see Supplementary Information for statistical validation). Lévy flights are characterized by a high degree of intrinsic heterogeneity, raising the possibility that equation (2) could emerge from an ensemble of identical agents, each following a Lévy trajectory. Therefore, we determined $P(r_g)$ for an ensemble of agents following a random walk (RW), Lévy flight (LF) or truncated Lévy flight (TLF) (Fig. 1d)[8,12,13]. We found that an ensemble of Lévy agents display a significant degree of heterogeneity in r_g; however, this was not sufficient to explain the truncated power-law distribution $P(r_g)$ exhibited by the mobile phone users. Taken together, Fig. 1c and d suggest that the difference in the range of typical mobility patterns of individuals (r_g) has a strong impact on the truncated Lévy behaviour seen in equation (1), ruling out hypothesis A.

If individual trajectories are described by an LF or TLF, then the radius of gyration should increase with time as $r_g(t) \sim t^{3/(2+\beta)}$ (ref. 21), whereas, for an RW, $r_g(t) \sim t^{1/2}$; that is, the longer we observe a user, the higher the chance that she/he will travel to areas not visited before. To check the validity of these predictions, we measured the time dependence of the radius of gyration for users whose gyration radius would be considered small ($r_g(T) \leq 3$ km), medium ($20 < r_g(T) \leq 30$ km) or large ($r_g(T) > 100$ km) at the end of our observation period ($T = 6$ months). The results indicate that the time dependence of the average radius of gyration of mobile phone users is better approximated by a logarithmic increase, not only a manifestly slower dependence than the one predicted by a power law but also one that may appear similar to a saturation process (Fig. 2a and Supplementary Fig. 4).

In Fig. 2b, we chose users with similar asymptotic $r_g(T)$ after $T = 6$ months, and measured the jump size distribution $P(\Delta r|r_g)$ for each group. As the inset of Fig. 2b shows, users with small r_g travel mostly over small distances, whereas those with large r_g tend to display a combination of many small and a few larger jump sizes. Once we rescaled the distributions with r_g (Fig. 2b), we found that the data collapsed into a single curve, suggesting that a single jump size distribution characterizes all users, independent of their r_g. This indicates that $P(\Delta r|r_g) \sim r_g^{-\alpha} F(\Delta r/r_g)$, where $\alpha \approx 1.2 \pm 0.1$ and $F(x)$ is an r_g-independent function with asymptotic behaviour, that is, $F(x) \sim x^{-\alpha}$ for $x < 1$ and $F(x)$ rapidly decreases for $x \gg 1$. Therefore, the travel patterns of individual users may be approximated by a Lévy flight up to a distance characterized by r_g. Most important, however, is the fact that the individual trajectories are bounded beyond r_g; thus, large displacements, which are the source of the distinct and anomalous nature of Lévy flights, are statistically absent. To understand the relationship between the different exponents, we note that the measured probability distributions are related

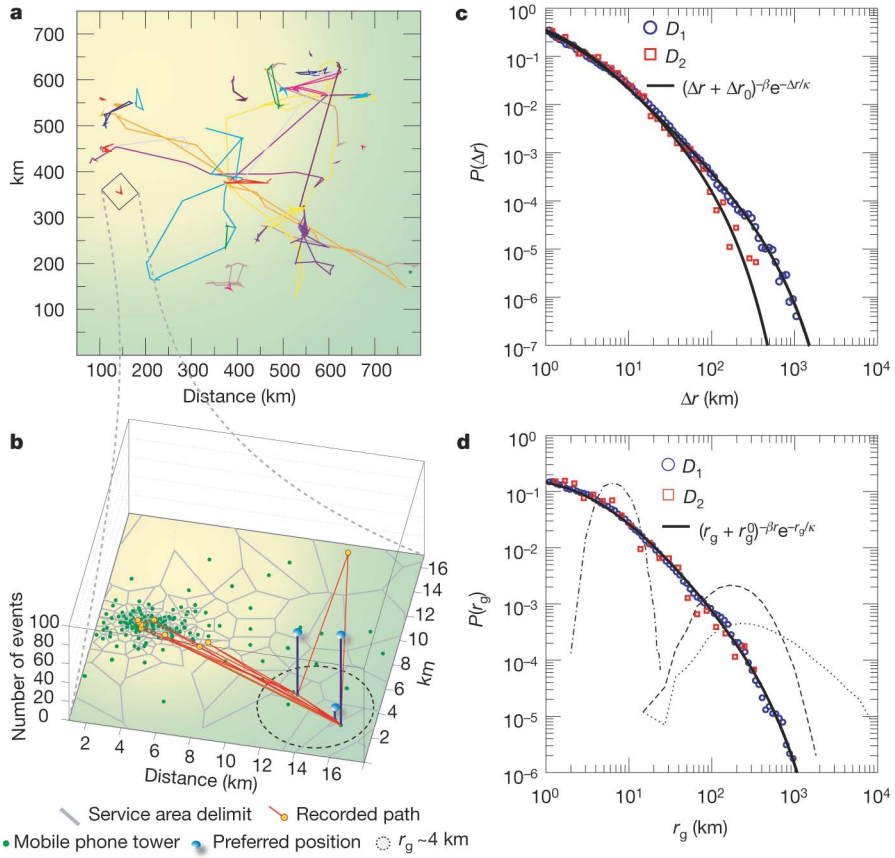

Figure 1 | Basic human mobility patterns. a, Week-long trajectory of 40 mobile phone users indicates that most individuals travel only over short distances, but a few regularly move over hundreds of kilometres. **b**, The detailed trajectory of a single user. The different phone towers are shown as green dots, and the Voronoi lattice in grey marks the approximate reception area of each tower. The data set studied by us records only the identity of the closest tower to a mobile user; thus, we can not identify the position of a user within a Voronoi cell. The trajectory of the user shown in **b** is constructed from 186 two-hourly reports, during which the user visited a total of 12 different locations (tower vicinities). Among these, the user is found on 96 and 67 occasions in the two most preferred locations; the frequency of visits for each location is shown as a vertical bar. The circle represents the radius of gyration centred in the trajectory's centre of mass. **c**, Probability density function $P(\Delta r)$ of travel distances obtained for the two studied data sets D_1 and D_2. The solid line indicates a truncated power law for which the parameters are provided in the text (see equation (1)). **d**, The distribution $P(r_g)$ of the radius of gyration measured for the users, where $r_g(T)$ was measured after $T = 6$ months of observation. The solid line represents a similar truncated power-law fit (see equation (2)). The dotted, dashed and dot-dashed curves show $P(r_g)$ obtained from the standard null models (RW, LF and TLF, respectively), where for the TLF we used the same step size distribution as the one measured for the mobile phone users.

©2008 Nature Publishing Group

by $P(\Delta r) = \int_0^\infty P(\Delta r|r_g)P(r_g)\,dr_g$, which suggests (see Supplementary Information) that up to the leading order we have $\beta = \beta_r + \alpha - 1$, consistent, within error bars, with the measured exponents. This indicates that the observed jump size distribution $P(\Delta r)$ is in fact the convolution between the statistics of individual trajectories $P(\Delta r_g|r_g)$ and the population heterogeneity $P(r_g)$, consistent with hypothesis C.

To uncover the mechanism stabilizing r_g, we measured the return probability for each individual $F_{pt}(t)$ (first passage time probability)[21,22], defined as the probability that a user returns to the position where he/she was first observed after t hours (Fig. 2c). For a two-dimensional random walk, $F_{pt}(t)$ should follow $\sim 1/(t\ln^2(t))$ (ref. 21). In contrast, we found that the return probability is characterized by several peaks at 24 h, 48 h and 72 h, capturing a strong tendency of humans to return to locations they visited before, describing the recurrence and temporal periodicity inherent to human mobility[23,24].

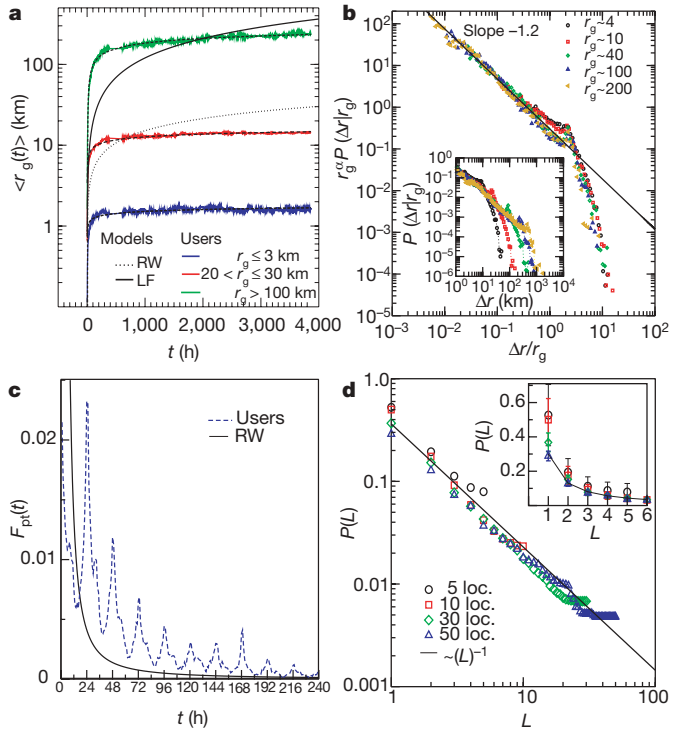

Figure 2 | The bounded nature of human trajectories. a, Radius of gyration $\langle r_g(t)\rangle$ versus time for mobile phone users separated into three groups according to their final $r_g(T)$, where $T = 6$ months. The black curves correspond to the analytical predictions for the random walk models, increasing with time as $\langle r_g(t)\rangle|_{LF,TLF} \sim t^{3/2+\beta}$ (solid curve) and $\langle r_g(t)\rangle|_{RW} \sim t^{0.5}$ (dotted curve). The dashed curves corresponding to a logarithmic fit of the form $A + B\ln(t)$, where A and B are time-independent coefficients that depend on r_g. **b**, Probability density function of individual travel distances $P(\Delta r|r_g)$ for users with $r_g = 4$, 10, 40, 100 and 200 km. As the inset shows, each group displays a quite different $P(\Delta r|r_g)$ distribution. After rescaling the distance and the distribution with r_g (main panel), the different curves collapse. The solid line (power law) is shown as a guide to the eye. **c**, Return probability distribution, $F_{pt}(t)$. The prominent peaks capture the tendency of humans to return regularly to the locations they visited before, in contrast with the smooth asymptotic behaviour $\sim 1/(t\ln(t)^2)$ (solid line) predicted for random walks. **d**, A Zipf plot showing the frequency of visiting different locations (loc.). The symbols correspond to users that have been observed to visit $n_L = 5$, 10, 30 and 50 different locations. Denoting with (L), the rank of the location listed in the order of the visit frequency, the data are well approximated by $R(L) \sim L^{-1}$. The inset is the same plot in linear scale, illustrating that 40% of the time individuals are found at their first two preferred locations; bars indicate the standard error.

To explore if individuals return to the same location over and over, we ranked each location on the basis of the number of times an individual was recorded in its vicinity, such that a location with $L = 3$ represents the third-most-visited location for the selected individual. We find that the probability of finding a user at a location with a given rank L is well approximated by $P(L) \sim 1/L$, independent of the number of locations visited by the user (Fig. 2d). Therefore, people devote most of their time to a few locations, although spending their remaining time in 5 to 50 places, visited with diminished regularity. Therefore, the observed logarithmic saturation of $r_g(t)$ is rooted in the high degree of regularity in the daily travel patterns of individuals, captured by the high return probabilities (Fig. 2b) to a few highly frequented locations (Fig. 2d).

An important quantity for modelling human mobility patterns is the probability density function $\Phi_a(x, y)$ to find an individual a in a given position (x, y). As it is evident from Fig. 1b, individuals live and travel in different regions, yet each user can be assigned to a well defined area, defined by home and workplace, where she or he can be found most of the time. We can compare the trajectories of different users by diagonalizing each trajectory's inertia tensor, providing the probability of finding a user in a given position (see Fig. 3a) in the user's intrinsic reference frame (see Supplementary Information for the details). A striking feature of $\Phi(x, y)$ is its prominent spatial anisotropy in this intrinsic reference frame (note the different scales in Fig. 3a); we find that the larger an individual's r_g, the more pronounced is this anisotropy. To quantify this effect, we defined the anisotropy ratio $S \equiv \sigma_y/\sigma_x$, where σ_x and σ_y represent the standard deviation of the trajectory measured in the user's intrinsic reference frame (see Supplementary Information). We found that S decreases monotonically with r_g (Fig. 3c), being well approximated with $S \sim r_g^{-\eta}$ for $\eta \approx 0.12$. Given the small value of the scaling exponent, other functional forms may offer an equally good fit; thus, mechanistic models are required to identify if this represents a true scaling law or only a reasonable approximation to the data.

To compare the trajectories of different users, we removed the individual anisotropies, rescaling each user trajectory with its respective σ_x and σ_y. The rescaled $\tilde{\Phi}(x/\sigma_x, y/\sigma_y)$ distribution (Fig. 3b) is similar for groups of users with considerably different r_g, that is, after the anisotropy and the r_g dependence are removed all individuals seem to follow the same universal $\tilde{\Phi}(\tilde{x}, \tilde{y})$ probability distribution. This is particularly evident in Fig. 3d, where we show the cross section of $\tilde{\Phi}(x/\sigma_x, 0)$ for the three groups of users, finding that apart from the noise in the data the curves are indistinguishable.

Taken together, our results suggest that the Lévy statistics observed in bank note measurements capture a convolution of the population heterogeneity shown in equation (2) and the motion of individual users. Individuals display significant regularity, because they return to a few highly frequented locations, such as home or work. This regularity does not apply to the bank notes: a bill always follows the trajectory of its current owner; that is, dollar bills diffuse, but humans do not.

The fact that individual trajectories are characterized by the same r_g-independent two-dimensional probability distribution $\tilde{\Phi}(x/\sigma_x, y/\sigma_y)$ suggests that key statistical characteristics of individual trajectories are largely indistinguishable after rescaling. Therefore, our results establish the basic ingredients of realistic agent-based models, requiring us to place users in number proportional with the population density of a given region and assign each user an r_g taken from the observed $P(r_g)$ distribution. Using the predicted anisotropic rescaling, combined with the density function $\tilde{\Phi}(x, y)$, the shape of which is provided as Supplementary Table 1, we can obtain the likelihood of finding a user in any location. Given the known correlations between spatial proximity and social links, our results could help quantify the role of space in network development and evolution[25–29] and improve our understanding of diffusion processes[8,30].

©2008 Nature Publishing Group

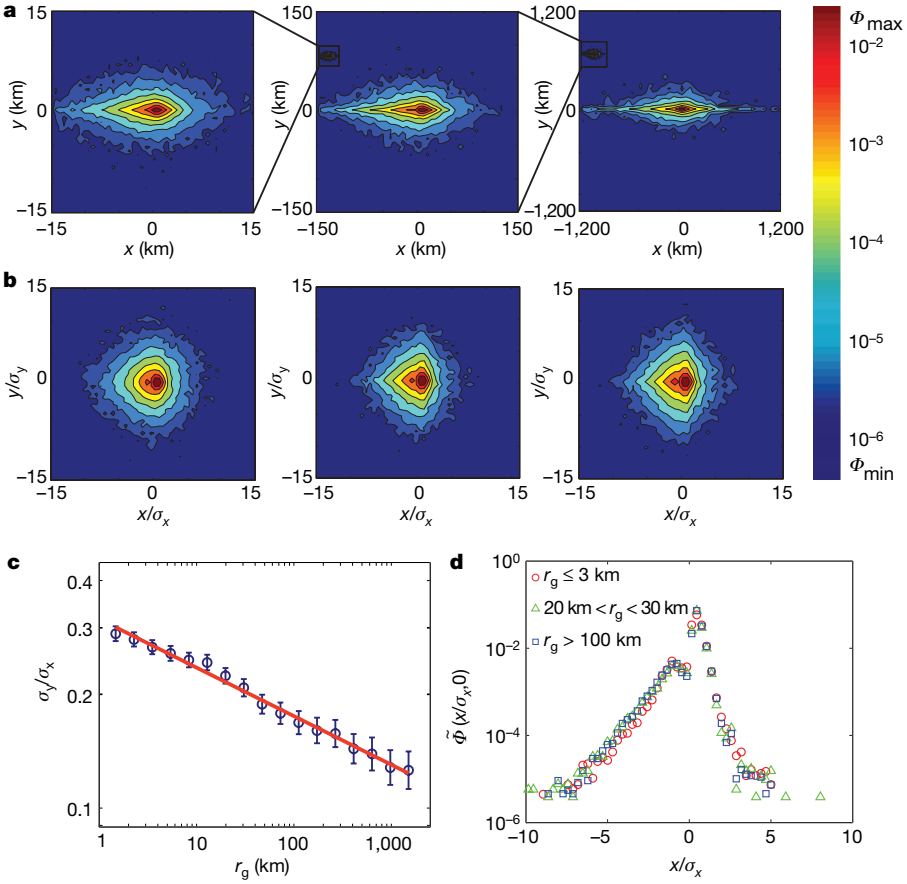

Figure 3 | The shape of human trajectories. **a**, The probability density function $\Phi(x, y)$ of finding a mobile phone user in a location (x, y) in the user's intrinsic reference frame (see Supplementary Information for details). The three plots, from left to right, were generated for 10,000 users with: $r_g \leq 3$, $20 < r_g \leq 30$ and $r_g > 100$ km. The trajectories become more anisotropic as r_g increases. **b**, After scaling each position with σ_x and σ_y, the resulting $\tilde{\Phi}(x/\sigma_x, y/\sigma_y)$ has approximately the same shape for each group. **c**, The change in the shape of $\Phi(x, y)$ can be quantified calculating the isotropy ratio $S \equiv \sigma_y/\sigma_x$ as a function of r_g, which decreases as $S \sim r_g^{-0.12}$ (solid line). Error bars represent the standard error. **d**, $\tilde{\Phi}(x/\sigma_x, 0)$ representing the x-axis cross-section of the rescaled distribution $\tilde{\Phi}(x/\sigma_x, y/\sigma_y)$ shown in **b**.

Received 19 December 2007; accepted 27 March 2008.

1. Horner, M. W. & O'Kelly, M. E. S Embedding economies of scale concepts for hub networks design. *J. Transp. Geogr.* **9,** 255–265 (2001).
2. Kitamura, R., Chen, C., Pendyala, R. M. & Narayaran, R. Micro-simulation of daily activity-travel patterns for travel demand forecasting. *Transportation* **27,** 25–51 (2000).
3. Colizza, V., Barrat, A., Barthélémy, M., Valleron, A.-J. & Vespignani, A. Modeling the worldwide spread of pandemic influenza: baseline case and containment interventions. *PLoS Medicine* **4,** 95–110 (2007).
4. Eubank, S. *et al.* Controlling epidemics in realistic urban social networks. *Nature* **429,** 180–184 (2004).
5. Hufnagel, L., Brockmann, D. & Geisel, T. Forecast and control of epidemics in a globalized world. *Proc. Natl Acad. Sci. USA* **101,** 15124–15129 (2004).
6. Kleinberg, J. The wireless epidemic. *Nature* **449,** 287–288 (2007).
7. Brockmann, D. D., Hufnagel, L. & Geisel, T. The scaling laws of human travel. *Nature* **439,** 462–465 (2006).
8. Havlin, S. & Ben-Avraham, D. Diffusion in disordered media. *Adv. Phys.* **51,** 187–292 (2002).
9. Viswanathan, G. M. *et al.* Lévy flight search patterns of wandering albatrosses. *Nature* **381,** 413–415 (1996).
10. Ramos-Fernandez, G. *et al.* Lévy walk patterns in the foraging movements of spider monkeys (*Ateles geoffroyi*). *Behav. Ecol. Sociobiol.* **273,** 1743–1750 (2004).
11. Sims, D. W. *et al.* Scaling laws of marine predator search behaviour. *Nature* **451,** 1098–1102 (2008).
12. Klafter, J., Shlesinger, M. F. & Zumofen, G. Beyond brownian motion. *Phys. Today* **49,** 33–39 (1996).
13. Mantegna, R. N. & Stanley, H. E. Stochastic process with ultraslow convergence to a gaussian: the truncated Lévy flight. *Phys. Rev. Lett.* **73,** 2946–2949 (1994).
14. Edwards, A. M. *et al.* Revisiting Lévy flight search patterns of wandering albatrosses, bumblebees and deer. *Nature* **449,** 1044–1049 (2007).
15. Sohn, T. *et al.* in *Proc. 8th Int. Conf. UbiComp 2006* 212–224 (Springer, Berlin, 2006).
16. Onnela, J.-P. *et al.* Structure and tie strengths in mobile communication networks. *Proc. Natl Acad. Sci. USA* **104,** 7332–7336 (2007).
17. González, M. C. & Barabási, A.-L. Complex networks: from data to models. *Nature Physics* **3,** 224–225 (2007).
18. Palla, G., Barabási, A.-L. & Vicsek, T. Quantifying social group evolution. *Nature* **446,** 664–667 (2007).
19. Hidalgo, C. A. & Rodriguez-Sickert, C. The dynamics of a mobile phone network. *Physica A* **387,** 3017–3024 (2008).
20. Barabási, A.-L. The origin of bursts and heavy tails in human dynamics. *Nature* **435,** 207–211 (2005).
21. Redner, S. *A Guide to First-Passage Processes* (Cambridge Univ. Press, Cambridge, UK, 2001).
22. Condamin, S., Bénichou, O., Tejedor, V. & Klafter, J. First-passage times in complex scale-invariant media. *Nature* **450,** 77–80 (2007).
23. Schlich, R. & Axhausen, K. W. Habitual travel behaviour: evidence from a six-week travel diary. *Transportation* **30,** 13–36 (2003).
24. Eagle, N. & Pentland, A. Eigenbehaviours: identifying structure in routine. *Behav. Ecol. Sociobiol.* (in the press).
25. Yook, S.-H., Jeong, H. & Barabási, A. L. Modeling the Internet's large-scale topology. *Proc. Natl Acad. Sci. USA* **99,** 13382–13386 (2002).
26. Caldarelli, G. *Scale-Free Networks: Complex Webs in Nature and Technology*. (Oxford Univ. Press, New York, 2007).
27. Dorogovtsev, S. N. & Mendes, J. F. F. *Evolution of Networks: From Biological Nets to the Internet and WWW* (Oxford Univ. Press, New York, 2003).
28. Song, C. M., Havlin, S. & Makse, H. A. Self-similarity of complex networks. *Nature* **433,** 392–395 (2005).
29. González, M. C., Lind, P. G. & Herrmann, H. J. A system of mobile agents to model social networks. *Phys. Rev. Lett.* **96,** 088702 (2006).
30. Cecconi, F., Marsili, M., Banavar, J. R. & Maritan, A. Diffusion, peer pressure, and tailed distributions. *Phys. Rev. Lett.* **89,** 088102 (2002).

Supplementary Information is linked to the online version of the paper at www.nature.com/nature.

Acknowledgements We thank D. Brockmann, T. Geisel, J. Park, S. Redner, Z. Toroczkai, A. Vespignani and P. Wang for discussions and comments on the manuscript. This work was supported by the James S. McDonnell Foundation 21st Century Initiative in Studying Complex Systems, the National Science Foundation within the DDDAS (CNS-0540348), ITR (DMR-0426737) and IIS-0513650 programs, and the US Office of Naval Research Award N00014-07-C. Data analysis was performed on the Notre Dame Biocomplexity Cluster supported in part by the NSF MRI grant number DBI-0420980. C.A.H. acknowledges support from the Kellogg Institute at Notre Dame.

Author Information Reprints and permissions information is available at www.nature.com/reprints. Correspondence and requests for materials should be addressed to A.-L.B. (alb@neu.edu).

©2008 Nature Publishing Group

ADDENDUM

doi:10.1038/nature07850

Understanding individual human mobility patterns

Marta C. González, César A. Hidalgo & Albert-László Barabási

Nature 453, 779–782 (2008)

The human mobility study relied on an anonymized billing dataset that was previously recorded by a mobile provider as required by law and billing purposes, and not for the purposes of this project. The research was reviewed and approved by the Institutional Review Board (IRB) at the US Office of Naval Research, the main sponsor of the project, and has approval from the Northeastern University's IRB as well, the institution where the work was carried out. As part of the IRB review, the first author, who handled the data, and the PI participated in ethics training sessions at the outset of the study.

©2009 Macmillan Publishers Limited. All rights reserved

doi: 10.1038/nature06958

SUPPLEMENTARY INFORMATION

Understanding individual human mobility patterns

Supplementary Material

Marta C. González, César A. Hidalgo, Albert-László Barabási

Contents

I. DATA

A. D_1 **Dataset**: This dataset was collected by a European mobile phone carrier for billing and operational purposes. It contains the date, time and coordinates of the phone tower routing the communication for each phone call and text message sent or received by 6 million costumers. The dataset summarizes 6 months of activity. To guarantee anonymity, each user is identified with a security key (hash code). Furthermore, we only know the coordinates of the tower routing the communication, hence a user's location is not known within a tower's service area. Each tower serves an area of approximately 3 km^2. Due to tower coverage limitations driven by geographical constraints and national frontiers no jumps exceeding $\sim 1,000$ km can be observed in the dataset.

The research was performed on a random set of $100,000$ selected from those making or receiving at least one phone call or SMS during the first and last month of the study, translating to $16,364,308$ recorded positions. We removed all jumps that took users outside the continental territory. We did not impose any additional criterion regarding the calling activity to avoid possible selection biases in the mobility pattern.

B. D_2 **Dataset:** Some services provided by the mobile phone carrier, like pollen and traffic forecasts, rely on the approximate knowledge of customer's location at all times of the day. For customers that signed up for location dependent services, the date, time and the closest tower coordinates are recorded on a regular basis, independent of their phone usage. We were provided such records for $1,000$ users, among which we selected the group of users whose coordinates were recorded at every two hours during an entire week, resulting in 206 users for which we have $10,613$ recorded positions. Given that these users were selected based on their actions (signed up to the service), in principle the sample cannot be considered unbiased, but we have not detected any particular bias for this data set.

For each user in D_1 and D_2 we sorted the time resolved sequence of positions and constructed individual trajectories.

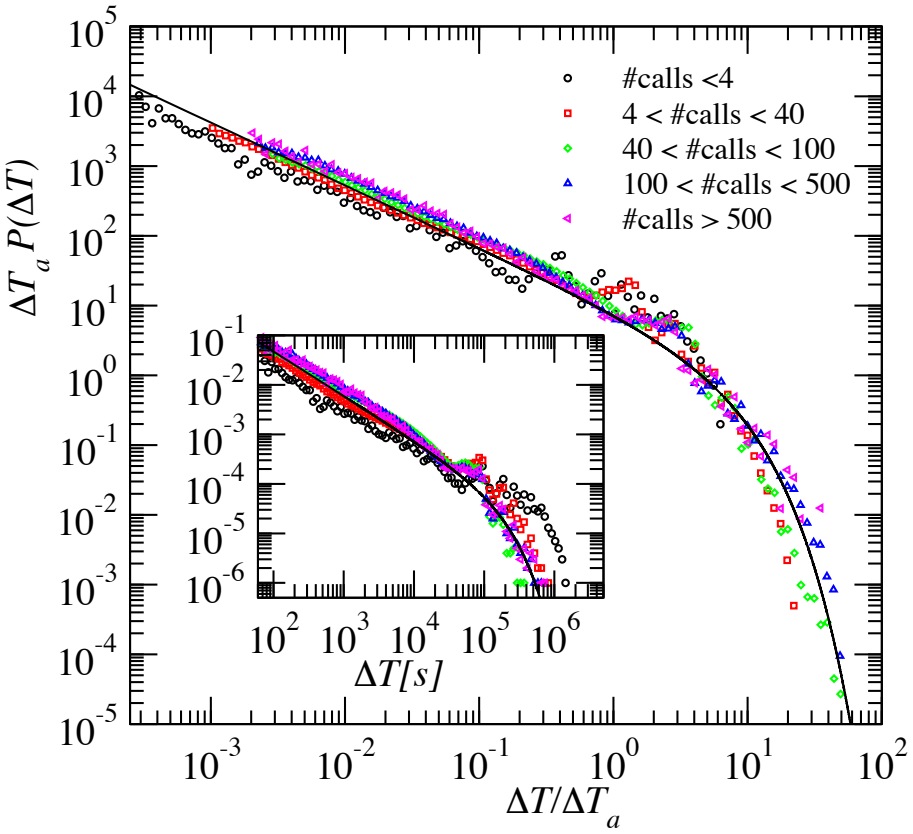

FIG. S1: Interevent time distribution $P(\Delta T)$ of calling activity. ΔT is the time elapsed between consecutive communication records (phone calls and SMS, sent or received) for the same user. Different symbols indicate the measurements done over groups of users with different activity levels (# calls). The inset shows the unscaled version of this plot. The solid line corresponds to Eq. (S1).

II. CHARACTERIZING INDIVIDUAL CALLING ACTIVITY

Communication patterns are known to be highly heterogeneous: some users rarely use the mobile phone while others make hundreds or even thousands of calls each month [1]. To characterize the dynamics of individual communication activity, we grouped users based on their total number of calls. For each user we measured the probability that the time interval between two consecutive calls is ΔT [2–4]. The inset of Fig. S1 shows that users with less activity tend to have longer waiting times between consecutive calls. By rescaling the axis with the average interevent time ΔT_a as $\Delta T_a P(\Delta T)$ and $\Delta T/\Delta T_a$ the obtained distributions collapse into a single curve (Fig. S1). Hence the measured interevent time distribution can be approximated by the expression $P(\Delta T)$

$= 1/\Delta T_a \mathcal{F}(\Delta T/\Delta T_a)$, where $\mathcal{F}(x)$ is independent of the average activity level of the population. This is a universal characteristic of the system and it agrees with earlier results on the temporal patterns of e-mail communication [5]. In addition, we find that the data in Fig. S1 is well approximated by

$$P(\Delta T) = (\Delta T)^{\alpha} \exp(\Delta T/\tau_c), \tag{S1}$$

where the power-law exponent $\alpha = 0.9 \pm 0.1$ is followed by an exponential cutoff of $\tau_c \approx 48$ days. Equation (S1) is shown by a solid line in the inset of Fig. S1 and its scaled version is presented in the main panel of Fig. S1. Here we used $\Delta T_a = 8.2$ hours, which is the average interevent time measured for the whole population. The heterogeneity in the communication pattern translates into heterogeneous sampling for the D_1 dataset. The D_2 dataset, with records at every two hours, obviously does not display this heterogeneity. Below we show that this temporal heterogeneity does not affect our results on the observed travel patterns.

III. OBSERVATIONS AT A FIXED INTEREVENT TIME

Given the widely varying distribution of the interevent times between two calls (an therefore the localization data), we need to investigate if the observed displacement statistics are affected by this sampling heterogeneity. Using the D_1 dataset, we calculated the displacement distribution $P(\Delta r)$ for consecutive calls separated by a time $\Delta T_o \pm 0.05 \Delta T_o$, where ΔT_o ranged from 20 min to one day. Figure S2 shows that for $\Delta T_o < 4$ h, the observed displacements are bounded by the maximum distance that users can travel in the ΔT_o time interval. For $\Delta T_o \geq 8$ hours we already observe $\Delta r_{max} \sim 1,000$ km, which corresponds to the largest displacement we could possible observe given the area under study (such large jumps likely are the result of airline travel). We observe that the resulting $P(\Delta r)$ distributions for different ΔT_o is again well approximated by a truncated power-law with an exponent $\beta = 1.75$. This agrees with the exponent found when we studied all consecutive calls (see Fig. 1C), suggesting that the use of consecutive calls is an accurate proxy to measure human displacement at large enough scales (> 1 km).

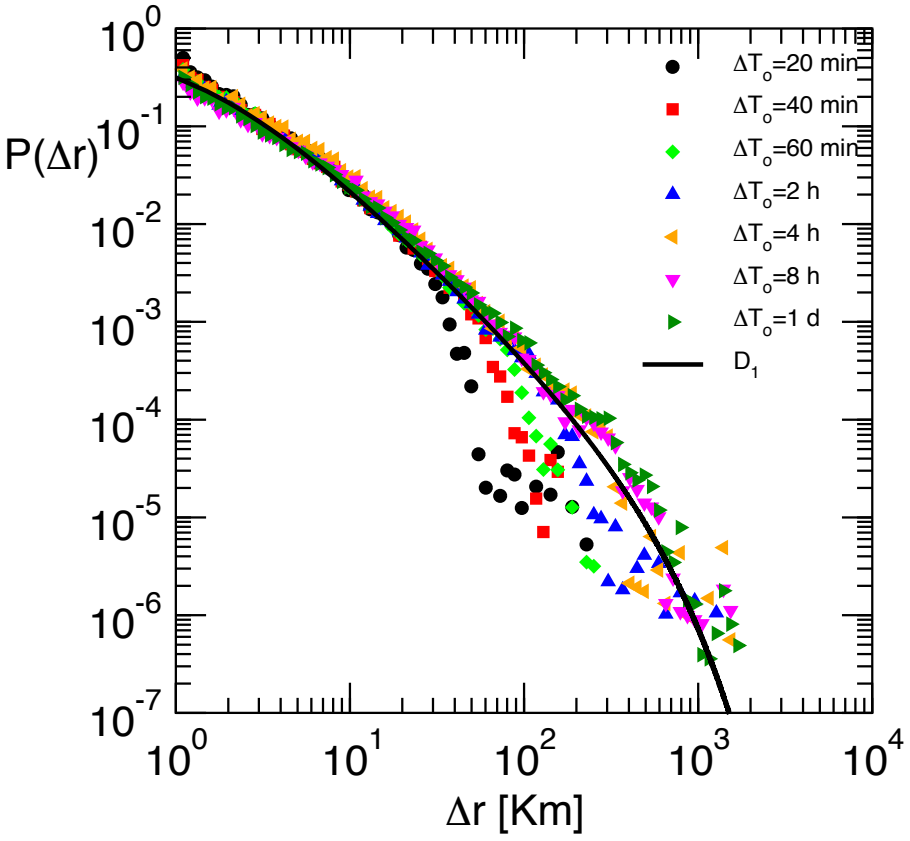

FIG. S2: Displacement distribution $P(\Delta r)$ for fixed inter event times ΔT_o based on the D_1 dataset. The cut-off of the distribution is set by the maximum distance users can travel for shorter inter event times, whereas for longer times the cutoff is given by the finite size of the studied area, as discussed in the manuscript. The black line is from (1) reported in the manuscript, with the value $\kappa = 400$ km corresponding to D_1 (solid line).

IV. INTRINSIC REFERENCE FRAME FOR INDIVIDUAL TRAJECTORIES

A. Radius of gyration: The linear size occupied by each user's trajectory up to time t is characterized by its the radius of gyration defined as

$$r_g^a(t) = \sqrt{\frac{1}{n_c^a(t)} \sum_{i=1}^{n_c^a} (\vec{r_i^a} - \vec{r}_{cm}^a)^2}, \tag{S2}$$

where $\vec{r_i^a}$ represents the $i = 1, ..., n_c^a(t)$ positions recorded for user a and $\vec{r}_{cm}^a = 1/n_c^a(t) \sum_{i=1}^{n_c^a} \vec{r_i^a}$ is the center of mass of the trajectory.

B. Moment of Inertia: To compare different users' trajectories we need to study them in a common reference frame. Inspired by the mechanics of rigid bodies [6], we assign each user to an intrinsic reference frame calculated a posteriori from a user's trajectory. We can think of the number times a user visited a given location as the mass associated with that particular position. We denote a user's trajectory with a set of locations $\{(x_1, y_1), (x_2, y_2), ...(x_{n_c}, y_{n_c})\}$, where n_c is the number of positions available for the user. An object's moment of inertia is given by the average spread of an object's mass from a given axis. A two dimensional object can be characterized by a 2×2 matrix known as the *tensor of inertia*

$$\mathbf{I} = \begin{pmatrix} I_{xx} & I_{xy} \\ I_{yx} & I_{yy} \end{pmatrix}. \tag{S3}$$

We can calculate the inertia tensor for user's trajectories by using the standard physical formulas

$$I_{xx} \equiv \sum_{i=1}^{n_c} y_i^2 \tag{S4}$$

$$I_{yy} \equiv \sum_{i=1}^{n_c} x_i^2 \tag{S5}$$

$$I_{xy} = I_{yx} \equiv -\sum_{i=1}^{n_c} x_i y_i. \tag{S6}$$

Since the tensor $\mathbf{I}$ is symmetric, it is possible to find a set of coordinates in which $\mathbf{I}$ will be diagonal. These coordinates are known as the tensor's principal axes $(\hat{e}_1, \hat{e}_2)$. In this set of coordinates $\mathbf{I}$ takes the form

$$\mathbf{I_D} = \begin{pmatrix} I_1 & 0 \\ 0 & I_2 \end{pmatrix}, \tag{S7}$$

where I_1 and I_2 are the principal moments of inertia. They also correspond to the eigenvalues of $\mathbf{I}$ and can be calculated from the original set of points as

$$I_1 = \frac{1}{2}(I_{xx} + I_{yy}) - \frac{1}{2}\mu \tag{S8}$$

$$I_2 = \frac{1}{2}(I_{xx} + I_{yy}) + \frac{1}{2}\mu, \tag{S9}$$

with

$$\mu \equiv \sqrt{4\, I_{xy}\, I_{yx} + {I_{xx}}^2 - 2\, I_{xx}\, I_{yy} + {I_{yy}}^2} \tag{S10}$$

The corresponding eigenvectors determine the principal axes ($\hat{e}_1$ and $\hat{e}_2$), representing the symmetry axes of a given trajectory.

C. Rotation of user trajectories: We transform each user's principal axes $(\hat{e}_1, \hat{e}_2)$ to a common intrinsic reference frame $(\hat{e}_x, \hat{e}_y)$ calculating the angle between the axes $\hat{e}_x$ and $\hat{e}_1$, as

$$\cos(\theta) = \frac{\vec{v}_1.\hat{e}_x}{|\vec{v}_1|} \tag{S11}$$

where v_1, is the eigenvector associated with the eigenvalue I_1

$$\vec{v}_1 = \begin{bmatrix} -\frac{I_{xy}}{1/2\, I_{xx} - 1/2\, I_{yy} + 1/2\, \mu} \\ 1 \end{bmatrix}, \tag{S12}$$

resulting in

$$\cos(\theta) = -I_{xy}\,(1/2\, I_{xx} - 1/2\, I_{yy} + 1/2\, \mu)^{-1}\, \frac{1}{\sqrt{1 + \frac{{I_{xy}}^2}{(1/2\, I_{xx} - 1/2\, I_{yy} + 1/2\, \mu)^2}}}. \tag{S13}$$

After rotation by θ, we impose a conditional rotation of 180^o such that the most frequent position lays always in $x > 0$.

D. Example: Figure S3 shows the recorded trajectories of 3 users (u_1, u_2 and u_3), each characterized by a different radius of gyration: $r_g|_{u1} = 2.28$ km, $r_g|_{u2} = 29.02$ km, and $r_g|_{u3} = 313.72$ km. Using (S4), (S5) and (S6), we calculated the different components of the tensor of inertia. Equations (S12) and (S13) allow us to determine the intrinsic axes for each user $(\hat{e}_1, \hat{e}_2)$, which are displayed in Fig. S3a. Their respective angles are: $\theta|_{u1} = 127.67^o$, $\theta|_{u2} = 40.20^o$ and $\theta|_{u3} = 60.08^o$. Each set of points is rotated by $-\theta$, such that $(\hat{e}_x, \hat{e}_y)$ is the new intrinsic reference frame of each user's trajectory, as shown in Fig. S3b. The most frequent and the second most frequent positions of each user are marked as a blue and orange circle respectively. After rotating the trajectory of user 2, its most frequent position lays in $x < 0$, hence we apply an additional rotation of 180^o such that the most frequent position lays in $x > 0$. The purpose of this is to conserve the asymmetry of the user's visitation pattern. In the absence of the rotation the trajectories in Fig. S3a and B (also Fig. 3 in the manuscript) will appear to be symmetric. Given, however, that there is a significant difference in the most and the second most visited locations (see Fig. 2D in the paper), we need to perform the symmetry breaking rotation to emphasize its presence. For example, we

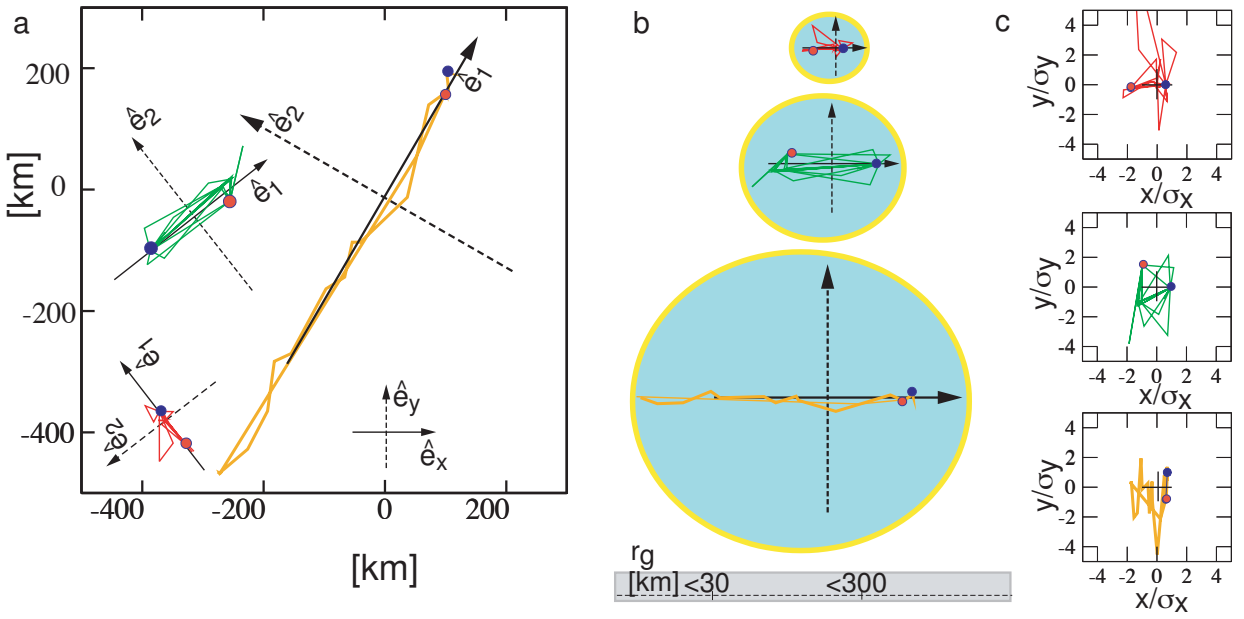

FIG. S3: Example of how to transform the user trajectories in a common reference frame. **a,** Initial trajectories of three users and their principal axes $(\hat{e}_1, \hat{e}_2)$. **b,** Each trajectory is rotated an angle $-\theta$ to align $\hat{e}_1$ with $\hat{e}_x$. An additional rotation with 180^o is required when the most frequent position (marked with a blue circle) lays in $x < 0$ after the rotation. This is the case of user 2 (green line). **c,** Positions (x, y) are scaled as $(x/\sigma_x, y/\sigma_y)$ after which the different trajectories have a quite similar shape.

found that for finite Lévy flights the rotation induced a slight but detectable anisotropy, capturing the fact that each finite trajectory has some inherent anisotropy.

We scale the trajectories on the intrinsic axes with the standard deviation of the locations for each user a

$$\sigma_x^a = \sqrt{\frac{1}{n_c^a}\sum_{i=1}^{n_c^a}(x_i^a - x_{cm}^a)^2}, \tag{S14}$$

$$\sigma_y^a = \sqrt{\frac{1}{n_c^a}\sum_{i=1}^{n_c^a}(y_i^a - y_{cm}^a)^2}. \tag{S15}$$

Note that the coordinate origin for each user is placed at the center of mass of the trajectory, $\vec{r_{cm}^a} = (0, 0)$. In this example, $\sigma_x|_{u1} = 2.24$ km, $\sigma_x|_{u2} = 28.76$ km, and $\sigma_x|_{u3} = 313.60$ km whereas $\sigma_y|_{u1} = 0.43$ km, $\sigma_y|_{u2} = 3.88$ km, and $\sigma_y|_{u3} = 8.49$ km. After scaling, the shapes of the three trajectories look similar (S3c), despite that we are showing users with significantly different mobility patterns and ranges. This is the underlying procedure that allows us to obtain

the universal density function $\tilde{\Phi}(x/\sigma_x, y/\sigma_y)$.

E. Spatial density function: For agent based modeling it is crucial to know the probability that an individual can be found at a position (x, y) during the day. As our results show, knowledge of the spatial density function $\tilde{\Phi}(x/\sigma_x, y/\sigma_y)$ represent the first step towards such a modeling effort. Indeed, using the density function $\tilde{\Phi}(x/\sigma_x, y/\sigma_y)$ for an ensemble of agents with r_g's following Eq.(3), each agent's position can be rescaled using Eq.(4) and the fact that $\sigma_x = 0.94 r_g^{0.97}$. The distribution of individuals in space can be arbitrary or more realistic if taken from census information. The three matrixes shown in Fig. 3B can be downloaded from: http://www.nd.edu/ mgonza16/DensityFunction/

V. SCALING RELATION BETWEEN EXPONENTS

Next we show that there is a consistent relationship among the different exponents describing the travel patterns of the population. The exponent β characterizing the distances traveled by the entire population is related to α, which characterizes distances traveled by individuals and β_r, that captures the distribution of the radius of gyration. We note that (1) should be the result of a convolution between (3) and $P(\Delta r|r_g)$, hence

$$P(\Delta r) = \int_0^\infty P(\Delta r|r_g) P(r_g) dr_g, \tag{S16}$$

using the expressions introduced in the manuscript this equation can be expanded as

$$P(\Delta r) = \int_0^\infty r_g^{-\alpha} F(\frac{\Delta r}{r_g})(r_g + r_g^0) e^{-r_g/\kappa} dr_g. \tag{S17}$$

Focusing on the asymptotic scaling behavior we drop the short length cutoff r_g^0 and extract the leading term by performing the substitution $r_g = \Delta r x$. Finally the scaling is given by

$$P(\Delta r) \approx \Delta r^{-\alpha-\beta_r+1} \int_0^\infty x^{-\alpha} F(\frac{1}{x}) e^{x\Delta r/\kappa} dx, \tag{S18}$$

indicating that $\beta = \alpha + \beta_r - 1$. Note, however, that the integral in (S18) also depends on Δr, therefore the scaling relationship is valid only to the leading order and further corrections may result from the integral. This correction cannot be evaluated in the absence of an analytical approximation for $F(x)$. For our data we find $\beta = 1.75 \pm 0.15$, $\beta_r = 1.65 \pm 0.15$ and $\alpha = 1.2 \pm 0.1$, indicating that the scaling relation, within error bars, is satisfied, and that there is a systematic difference between β and β_r of magnitude $\alpha - 1$.

VI. TIME DEPENDENCE OF THE RADIUS OF GYRATION

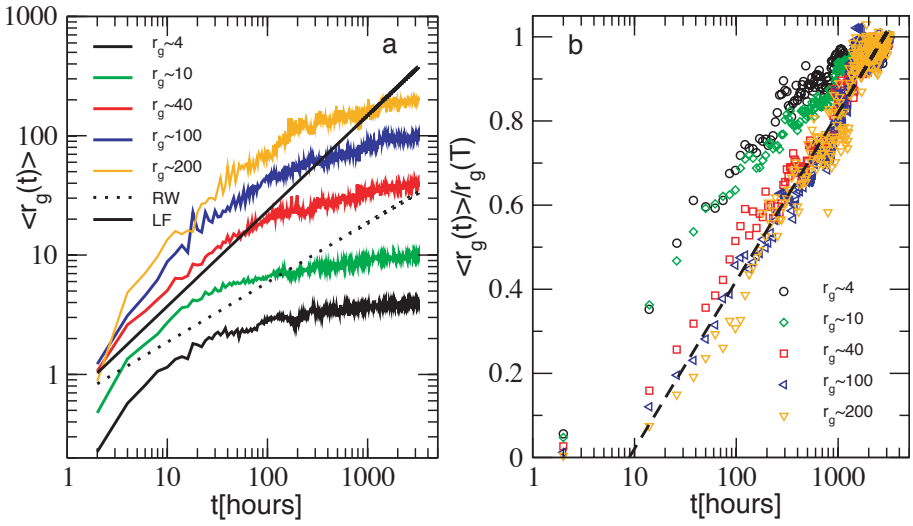

FIG. S4: Time evolution of the radius of gyration $\langle r_g(t)\rangle$ vs. time, for various groups of users with different asymptotic $r_g(T)$ after $T = 6$ months. **a,** In a log-log scale the black lines correspond to the powers of time for the random walk and Lévy flight models, which are in contrast with the time dependence of $\langle r_g(t)\rangle$ measured for the mobile phone users. **b,** In a log-linear scale, note that the $r_g = 4$ and $r_g = 10$ visibly deviate from the large r_g curves. This is not surprising, as for these two curves the recorded distances are comparable to the average tower distances (both curves appear to saturate under 10 km, while the average area of reception for a tower is about 3 km^2). Thus, small travel distances are overestimated due to the measurement resolution. Curves with $r_g > 10$ km are less affected by the tower resolution and all these appear to collapse in the same behavior once rescaled with $r_g(T)$, and they are all approximated with a logarithmic time dependence. The straight line is not a fit, but it is shown only as a guide to the eye.

Figure 2A in the manuscript shows three groups of users chosen according to the asymptotic $r_g(T)$ after $T = 6$ months. In Fig. S4 we show that the same time dependence is observed for a more strictly selected grouping of the users, choosing five different groups of users with very similar asymptotic radius of gyration: $r_g(T) \pm 0.05 r_g(T)$. Given the high daily and weekly-based

fluctuations in the phone usage patterns, we averaged $\langle r_g(t) \rangle$ over 168 different initial conditions, *i.e.* we started the measurements at every 6 hours during one week. This averaging not only removed the dependence on the initial conditions, but also significantly reduced the noise in the curves.

The log-log scale in Fig. S4a allows to see in detail the early behavior of the curves, indicating that a power law does not offer a good fit to the data. As we show in the log-linear plot in Fig. S4b, we find that the radius of gyration increases logarithmically in time, which is in strong contrast with the power law dependence expected for Lévy flights ($r_g(t)|_{LF/TLF} \sim t^{3/(2+\beta)}$) and random walks ($r_g(t)|_{RW} \sim t^{1/2}$). This indicates that the average radius of gyration of mobile phone users has a manifestly slower dependence than the predicted power laws, a behavior that may appear similar to a saturation process. Note that the $r_g \sim 4, 10$ curves appear to deviate from the logarithmic behavior. We belive that this is due to the spatial resolution offered by the tower density: we cannot reliably and systematically resolve jumps in the vicinity of a few kms, given that we record a motion only when a person moves between towers, that are often a few kilometers apart. The $r_g > 10$ km curves, given the distances involved, are not affected by the granularity of the data collection process, and they all follow the logarithmic behavior.

VII. STATISTICAL TESTS OF FITTING DISTRIBUTIONS

Given the fat tailed distributions observed for human travel patterns, it is important to see if the data is statistically consistent with the best fits. The purpose of this section is to support our findings with rigorous statistical tests. In the past year there has been significant attention devoted to the question of how to statistically measure the goodness of fit for a power law [7–10]. This was prompted partly by the need to quantify the validity of the Lévy flight finding in animal travel patterns. Note, however, that there is a significant difference between the data quality available in the animal and human travel patterns. Indeed, the mammalian data was available for short time periods for only a few animals, providing only a small number of observed individual displacements. Given the scarcity of data, precise statistical tools are needed to extract the proper fit. In contrast, the data analyzed in Ref. [11] as well as in this paper contain millions of displacements. Thus we are in a regime where typically traditional statistical tools, designed to deal with limited information, are less crucial. Yet, appropriate statistical tools can be used to explore the goodness

of the fit.

In this respect, it is often believed that statistical methods can validate a particular fit. The truth is, as emphasized in a recent publication [10], that these tools can only tell if a particular fit is consistent with the data, and rule some fits out, rather than validate a particular fit. A second important observation is that, given the high interest devoted to power laws, recently the issue of fitting a power law has been addressed in detail, developing the proper statistical tools to address the goodness of the fit [7–10]. The same tools are not available for truncated power laws, however, thus limiting the available methods to address their statistical relevance. In general we find that all the fits that we used in the paper pass the Kolmogorov-Smirnov test for the goodness of fit (Sect. V.A) and that a power law offers a much better approximation overall than an exponential function (Sect. V.B). Note that given the vast amount of data and the really good fit offered by the truncated power law, this last conclusion is hardly surprising.

A. Kolmogorov-Smirnov goodness of fit test

We tested whether the empirical data could come from the fitted distributions by performing a stringent variant of the Kolmogorov-Smirnov (KS) goodness of fit test [10]. The KS statistics is a simple way to compare whether two distributions are the same. In this case, we use it to test the hypothesis: *Could the empirically observed distributions come from the distribution found as its best fit*. For this we generated synthetic data starting from the fitted distribution and then use the KS test to see whether the empirical data we have behaves as well as the synthetic data generated from the fitted distribution.

We use two variants of the KS statistics to compare empirical data with the fitted distribution and synthetic data with the fitted distribution. The first method is the standard KS statistics and is given by:

$$KS = \max\left(|F - P|\right) \tag{S19}$$

where F is the cumulative distribution of the best fit and P is the cumulative distribution of the empirical or synthetic data. The regular KS statistic is not very sensitive on the edges of the cumulative distribution. Hence, we also used the weighted KS statistics defined as:

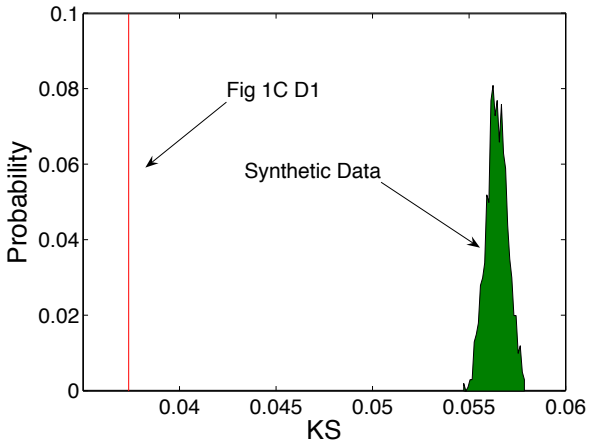

FIG. S5: KS test for Fig 1C D_1

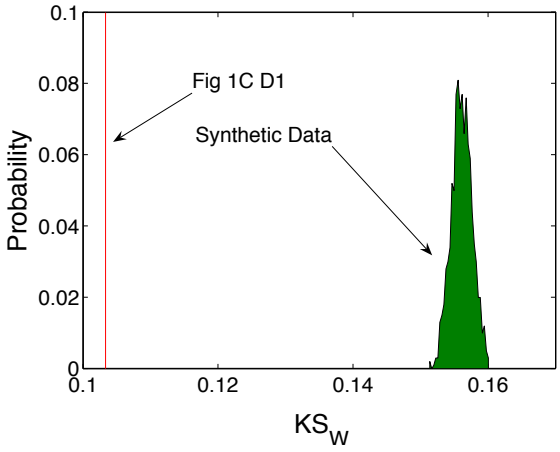

FIG. S6: KS_W test for Fig 1C D_1

$$KS_W = \max \frac{|F - P|}{\sqrt{P(1-P)}} \tag{S20}$$

To test whether the empirical data behaves as good as the synthetic data we calculated the KS and KS_W statistics between the empirical data and its best fit and compared these values with those obtained by calculating KS and KS_W for $1,000$ synthetic data sets generated from the best fit. If the values obtained for KS and KS_W for the empirical data behave as good or better than those obtained for the synthetic data, then we can conclude that the empirical data is statistically consistent with its best fit. The results of the KS test can be summarized using a $p - value$

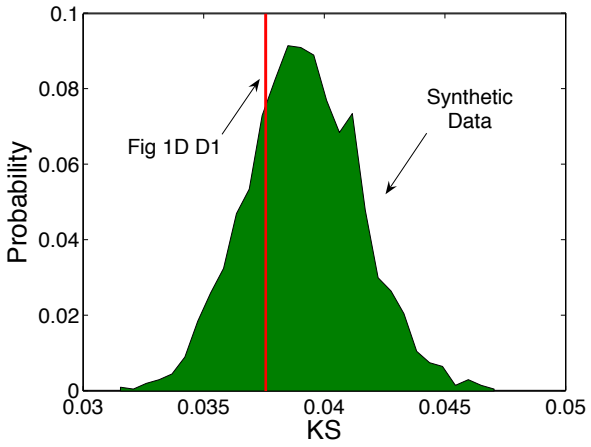

FIG. S7: KS test for Fig 1D D_1

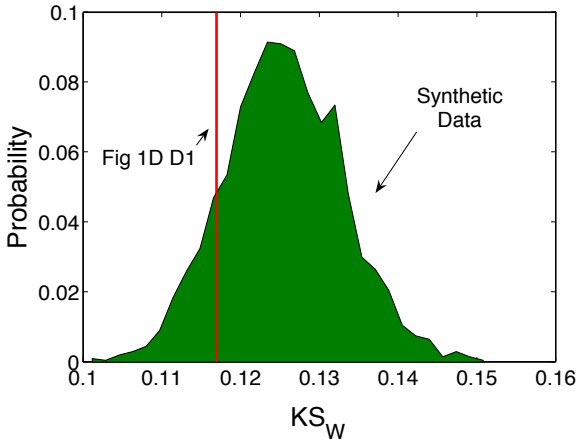

FIG. S8: KS_W test for Fig 1D D_1

by integrating the distribution of KS values generated with the synthetic data from the value representing the empirical distribution. When integrating such distributions from left to right we can interpret the $p-value$ as the probability that the observed data was the result of its best fit. A $p-value$ close to 1 will indicate that the empirical distribution matches its best fit as good as synthetic data generated from the fit itself [10], whereas a relative small $p-value$ (typically taken $p<0.01$) would suggest that the empirical distribution can not be the result of its best fit.

Passing the KS test does not rule out the possibility that the empirical data could be fitted as well or even better with some other function. In such a case, given the size of our samples, we

believe that such an exercise would be technical rather than practical and that different functional forms will closely resemble each other on the range were the fit was made once the fitting parameters have been fixed.

1. KS statistics for Fig 1C, D_1: Figure S5 compares the KS values obtained for the empirical data presented in Fig 1C, D_1 of the paper with those obtained for $1,000$ distributions of synthetic data generated to comply with Eq. (1). Figure S6 shows the same for KS_W. In both cases we find that the empirical data passes the KS test, in fact behaving better than the synthetic data. Indeed $p(KS) = 1$ and $p(KS_W) = 1$.

2. KS statistics for Fig 1D, D_1: Figure S7 compares the KS values obtained for the empirical data presented in Fig 1D, D_1 of the paper with those obtained for 2000 distributions of synthetic data generated to comply with Eq. (3). Figure S8 shows the same for KS_W. In both cases we find that the empirical data passes the KS test, behaving as some of the best examples of the synthetic data, obtaining $p(KS) = 0.62$ and $p(KS_W) = 0.82$.

B. Maximum Likelihood Estimates: Comparing power-laws and exponentials

The Maximum Likelihood Method is a powerful way of estimating the fitting parameters best describing a empirical distribution. The method can also be used to compare the relative likelihood of two fits. In this section we are interested in testing whether a broad distribution, such as a power-law, is a better fit than an exponential for many of the distributions presented on the paper. It is not our intention to claim that the distributions presented here are in fact power-laws but to build suggestive evidence testing if the data presented in the paper is better fitted by a broad distribution, such as the power-law, rather than a narrow distribution such as an exponential. In fact, as we discuss in the manuscript and the previous section, we believe that the best fit to our data is given by a truncated power law rather than a simple power law. We do not present here the maximum likehood estimate of the truncated power-law fit because being its cumulative a Whittaker function, it is not readily to be handled with this method. For those interested in the accuracy of the best fit we suggest reading section VII A of this supplementary material.

The details of the maximum likelihood method have been widely published. Those interested in performing such fits could find help in [10] and [7].

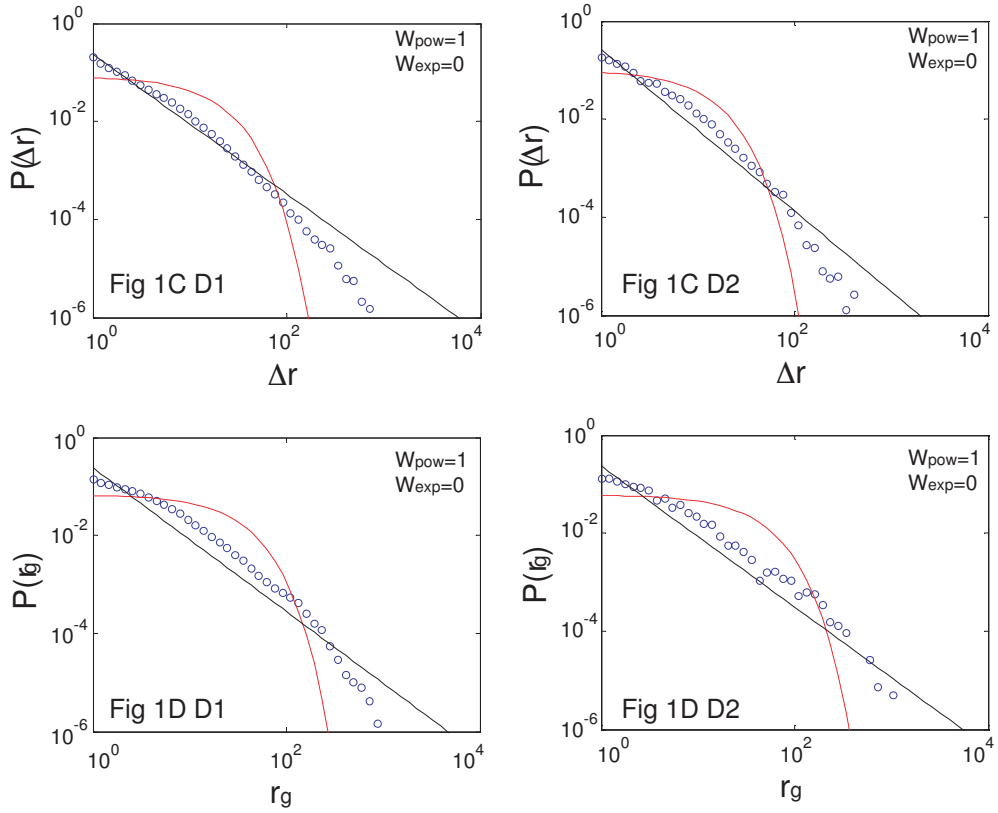

FIG. S9:

Testing for broad and narrow distributions: The relative likelihood between two distributions can be calculated from its relative weights

$$W_i = \frac{e^{-\Delta_i}}{e^{-\Delta_1} + e^{-\Delta_2}}, \tag{S21}$$

where $\Delta_i = \min\left(AIC_i - AIC_{min}\right)$. Here AIC is the Akaike information criteria associated with the power-law ($i = 1$) and exponential ($i = 2$) fits. The AIC can be expressed as a function of the log-likelihood [7]

$$AIC_i = 2\log\max(L_i) + 2K_i$$

where K_i is the number of parameters used in the fit and L_i is the likehood of a particular value of a fitting parameter.

Here we test two fits, a power-law $Ax^{-\beta}$ and an exponential $Ae^{-\mu x}$, where A is a normalization constant. In Fig. S9 we present the results of the Maximum Likelihood Fits for the distributions introduced in Fig. 1C and Fig. 1D of the paper. Note, we use the data log binned data, which has been recommended as the most accurate plotting method for this kind of analysis [8]. In each case we find $W_{pow} >> W_{exp}$ indicating that a power law is a more likely fit than an exponential, indicating that the distribution of displacements, as well as r_g, are better approximated by a broad rather than a narrow distribution.

[1] Onnela, J.-P., Saramäki, J., Hyvönen, J., Szabó, G., Lazer, D., Kaski, K., Kertész, K. & Barabási A.L. Structure and tie strengths in mobile communication networks. *Proceedings of the National Academy of Sciences of the United States of America* **104**, 7332-7336 (2007).

[2] Barabási, A.L. The origin of bursts and heavy tails in human dynamics. *Nature* **435**, 207-211 (2005).

[3] Vázquez, A., Oliveira, J.G., Dezsö, Z., Goh,K.-I, Kondor, I. & Barabási, A.-L. Modeling bursts and heavy tails in human dynamics. *Physical Review E* **73**, 036127 (2006).

[4] Hidalgo, C. & Barabási, A.L. Inter-event time of uncorrelated and seasonal systems. *Physica A* **369**, 877-883 (2007).

[5] Goh, K.-I. & Barabási, A.L. Burstiness and memory in complex systems. *Eurphysics Letters* **81** 48002 (2008).

[6] Goldstein, H. *Classical Mechanics*. (Addison-Wesley, 1959).

[7] Edwards, A.M., Phillips, R.A., Watkins,N.W., Freeman, M.P., Murphy, E.J., Afanasyev, V., Buldyrev, S.V., da Luz, M.G.E., Raposo, E. P., Stanley, H. E., & Viswanathan, G. M. Revisiting Lvy flight search patterns of wandering albatrosses, bumblebees and deer. *Nature* **449**, 1044-1049 (2007).

[8] Sims D.W., Righton D. & Pitchford, J.W. Minimizing errors in identifying Lévy flight behaviour of organisms. *Journal of Animal Ecology* **76**, 222-229 (2007).

[9] Pueyo, S. & Jovani, R. Comment on A keystone mutualism drives pattern in a power function. *Science* **313**, 1739c (2006).

[10] Clauset, A., Rohila Shalizi, C. & Newman, M.E.J. Power-law distributions in empirical data. *arXiv:physics:/07061062*.

[11] Brockmann, D., Hufnagel, L. & Geisel, T. The scaling laws of human travel. *Nature* **439**, 462-465 ,(2006).